Fast Algorithm for Rough-Surface Scene Simulation in Passive Millimeter Wave Imaging

CHUAN YIN, YOULIN GENG, YUJIAN PAN, AND HUAYAN JIN

College of Electronics and Information, Hangzhou Dianzi University, Hangzhou 310018, China

Corresponding author: Youlin Geng (gengyoulin@aliyun.com)

ABSTRACT Simulation in the passive millimeter-wave (MMW) imaging of rough surfaces is an indispensable step in the simulation in passive radiation imaging. The multi-layer brightness temperature tracing method (MBTTM) can be used to simulate the image of a rough surface, which has been proven in our previous work. However, it causes a significant decrease in efficiency of the simulation. To solve this problem, a fast MBTTM is proposed in this paper. In the new method, the uniformly emission method and multi-layer densification method are presented. To validate the correctness of the new algorithm, the comparison of the simulation and measurement results are proposed. These results are in good agreement, which indicates that the fast MBTTM can notably shorten the computing time of the simulation of the rough-surface scene.

INDEX TERMS MMW, rough surface, MBTTM, MLDM, UEM.

I. INTRODUCTION

Millimeter-wave (MMW) imaging has been a heavily researched topic in imaging work in recent years. A desirable advantage of MMW imaging is that millimeter-waves can penetrate cloud, mist, and dust [1]–[4]. Compared with active millimeter wave imaging, the passive MMW imaging is more widely used because of its good stealth in detecting and discriminating targets [5]–[11].

Currently, the work of passive MMW imaging is restricted by the imaging distance. At the beginning of the twenty-first century, with the development of advanced technology of large-field instantaneous imaging [12], [13], passive MMW remote sensing was also developed. Consequently, the simulation in passive MMW imaging was developed, which is of great value in the study of passive MMW radiation of various types of targets. First, it is helpful to recognize the radiation characteristics of the target, explain certain radiation phenomena, identify the specific radiation patterns and determine the measured results. Second, the simulation in passive MMW imaging is beneficial to the parameter design of the radiometer system, with which the performance and situation of the radiometer can be conveniently assessed. Finally, the passive MMW imaging sensor is state-of-the-art and expensive to date, and raw passive MMW image data of natural scenes are difficult to acquire under various conditions. Thus, the simulation of passive MMW has become an effective supplement and substitute for real measurements to save time and cost.

Simulation works of MMW imaging are reported in [14]–[18], but those works focus on the active MMW imaging. Passive MMW imaging simulation technology first appeared in Salmon [19], where plastic- and metal-object microwave imaging was simulated; however, only few specific objects are modeled in this paper. Next, a suitable general model for all simple scenes was established in [20], where the effect of single reflection was only considered, and the connection among the targets in the scene was not concerned. After that step, to simulate more complex scenes, a greater level of sophistication in the model was proposed in [21], where the interaction among various brightness temperature targets in the model was counted with the radiometric method. However, the interaction in the brightness temperature tracing method is counted with the ray-tracing method, which can adjust the resolution in a certain range to improve the flexibility [14], [22], [23]. Next, a passive MMW imaging system for remote sensing was developed in [24]. A fast ray-tracing method for passive MMW simulation was proposed in [25] to promote the efficiency, and a new simulation approach for passive MMW was presented in [26], which combined the ray-tracing method and

Huygens' Principle. Afterwards, the brightness temperature simulation in extremely rough surface imaging was obtained in [27] and [28], where the surface was approximated by Lambertian approximate law. In the previous work, we presented an improved model to simulate the rough-surface scene, and MBTTM was proposed to obtain the radiation brightness temperature of the rough surface [29]. An improved model to simulate the image of multi-layer rough surfaces was proposed in [30], which extended the applied range of the simulation in passive MMW. Unfortunately, the MBTTM must calculated more layers; therefore, it will significantly decrease the efficiency of the simulation.

The review leads us to the conclusion that a fast MBTTM is required to increase the simulation efficiency in complicated scenes with several rough surfaces. The principle of the MBTTM is introduced in detail in Section 2. In Section 3, the UEM and MLDM are proposed to reduce the number of sub-layer rays, which can also increase the usage of the rays. In Section 4, we use the fast MBTTM to simulate the actual scene to demonstrate the correctness of the proposed method, and the effect of two parameters on the simulation is discussed. Next, the conclusion follows in Section 5. The results imply that the fast MBTTM can significantly increase the efficiency of the MBTTM and reduce the calculation time.
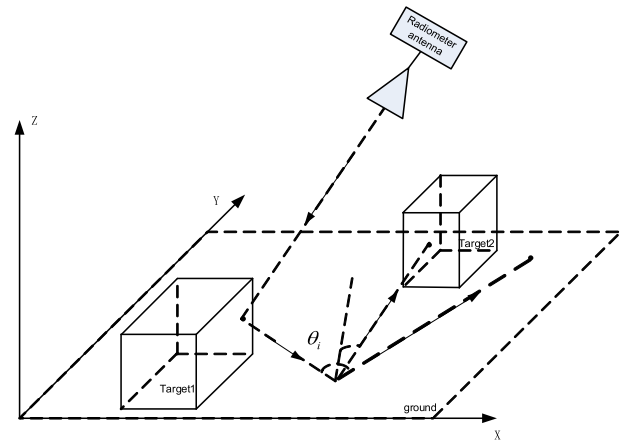

FIGURE 1. Schematic diagram of MBTTM.

II. PRINCIPLE OF THE FAST SIMULATION ALGORITHM

Compared with the single-layer brightness temperature tracing method, the diffuse reflection can be accounted in the MBTTM to simulate a rough surface. All rays are layered in the tracing, and the principle of layers relies on the time of the diffused reflection of the ray. For instance, the rays that do not experience the diffused reflection are considered the first layer, and the rays that experience the diffused reflection once are considered the second layer. The schematic diagram is shown in Figure 1.

We have demonstrated that the relative error of the result decreases with the number of layers, which increases the rays. The tracing model of MBTTM of a single ray is shown in Figure 2.

In Figure 2, a ray crosses the ground in the direction θ_i, the intersection point is considered a new source, and several rays scatter in several directions in the model.

In the calculation of the brightness temperature of the rough surface, the emissivity of the surface should be

FIGURE 2. Tracing model of MBTTM of a single ray.

obtained. For a smooth surface, the emissivity $e_{dp}(\theta_i)$ in direction θ_i is represented by [28], [31]

$$e_{dp}(\theta_i) = 1 - r_{dp}(\theta_i) - t_{dp}(\theta_i) \tag{1}$$

where $r_{dp}(\theta_i)$ and $t_{dp}(\theta_i)$ are the reflectivity and transmittance in the p polarization of the ground in direction θ_i. Unlike a smooth surface, the contribution of the non-reflection direction should be considered in calculating the emissivity of the rough surface; thus, we have [28]

$$e_{dp}(\theta_i) = 1 - r_{dp}^{co}(\theta_i) - r_{dp}^{non}(\theta_i) - t_{dp}(\theta_i) \tag{2}$$

where $r_{dp}^{co}(\theta_i)$ and $r_{dp}^{non}(\theta_i)$ are its coherent and non-coherent reflection coefficients, respectively. In this case, $t_{dp}(\theta_i)$ in (1) and (2) is 0. The former has been introduced above, and the latter is given by equation (3) [28].

$$
\begin{aligned}
r_{dp}^{non}&(\theta_i) \\
&= \iint_{\Omega} \frac{[\sigma_{pp}(\theta_i, \varphi_i; \theta_m, \varphi_n) + \sigma_{pq}(\theta_i, \varphi_i; \theta_m, \varphi_n)] \cdot \sin(\theta_m)}{4\pi \cos(\theta_i)} \\
&\quad \times d\theta_m d\varphi_n
\end{aligned}
\tag{3}
$$

where $\sigma_{pp}(\theta_i, \varphi_i; \theta_m, \varphi_n)$ is the bistatic scattering coefficient from direction (θ_m, φ_n) to (θ_i, φ_i) in the p polarization. we can conclude from (3) that the reflectivity in direction θ_i is the integral of the bistatic scattering coefficient on the half sphere surface. In the numerical calculation, the reflectivity is the sum of the reflectivities in different directions, which is the product of the bistatic scattering coefficient and weighting coefficient. The number of the rays is the number of items in the calculation. Obviously, the accuracy of the results increases with the number of rays. However, more rays will lead to extra computation. Hence, a new method to reduce the number of rays without decreasing the accuracy of results is required to reduce the computational complexity.

III. FAST MULTI-LAYER BRIGHTNESS TEMPERATURE TRACING METHOD

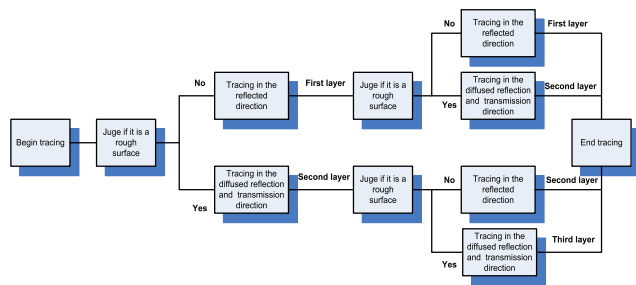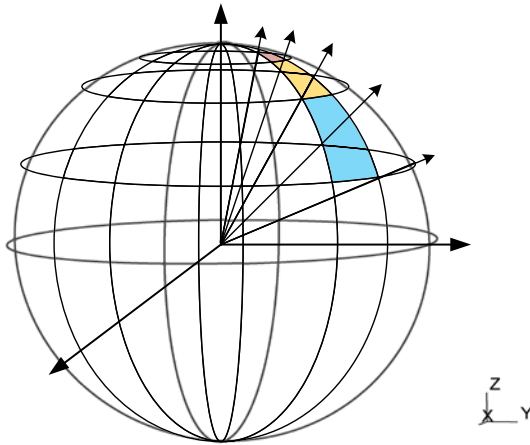The fast MBTTM contains two approaches: UEM and MLDM, whose details are as follows.

FIGURE 3. Traditional emission method.

A. UNIFORMLY EMISSION METHOD

First, we found that the mission method in the original MBTTM is not appropriate for a rough-surface scene. The traditional emission method is shown in Figure 3. The angle between the adjacent rays is clearly an invariant value, and the rays are not uniformly distributed on the sphere surface.

Assumed that θ is the angle between the ray and the Z axle. The density of the rays decreases with angle θ; therefore, the rays are sparsely distributed when angle θ is nearly 0 degree. Clearly, the traditional method is not appropriate to compute the emissivity of the rough surface.
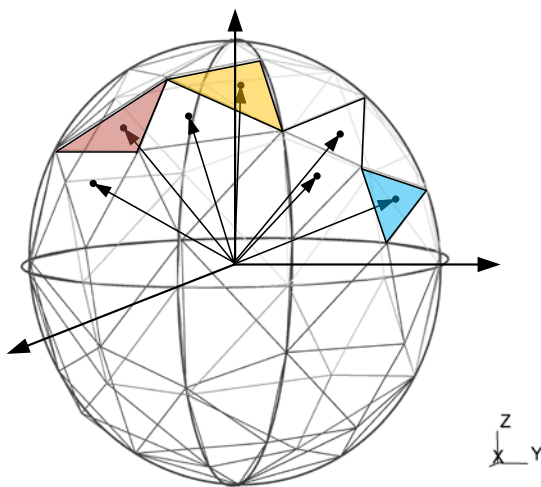

FIGURE 4. Model of triangle meshing on the sphere surface.

To solve this problem, an improved emission method called UEM is proposed in this paper. In the UEM, several seamless joint triangles are meshing on the sphere surface, as shown in Figure 4. The direction of each ray is the center of the triangle. Therefore, the rays are uniformly distributed on the sphere surface.

To demonstrate the effect of the improved method, two methods are used to calculate the same scene as shown in Figure 5.
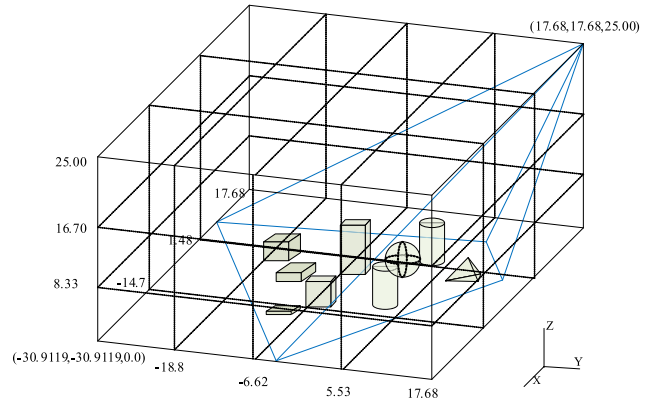

FIGURE 5. Three-dimension model of a virtual scene.

In Figure 5, the work frequency is 90 GHz, the model contains five hexahedrons of different sizes, a sphere, two cylinders, and a tetrahedral in different positions, all of which are located on the plane x-o-y. The permittivity of the hexahedrons and cylinders is set as $3.4 - j0.02$, the permittivity of the sphere and tetrahedral are set as $8.0 - j0.02$, and the permittivity of the bottom surface is set as $6.0 - j0.1$. The physical temperatures of the sky, targets and bottom surface are set as 50K, 300K and 250K, respectively. The radiometer is at the vertex, and the central direction of the scanning scope is defined by spherical angles $\theta = 45°$ and $\varphi = 45°$. However, the diffraction and transmission are not considered in the model. The simulated image of the scene is shown in Figure 6.
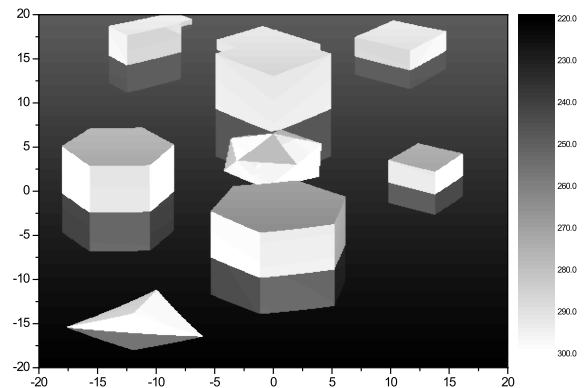

FIGURE 6. Simulated image of the scene.

The relative errors of the results are shown in Figure 7. The relative errors are obtained by

$$relative\ errors = \frac{\|A - B\|_f^2}{num} = \frac{\sqrt{\sum (a_{ij} - b_{ij})^2}}{num} \quad (4)$$

where A and B are the standard brightness temperature distribution matrix and evaluation matrix, and num is the number of matrix elements.

As shown in Figure 7, two curves represent the relative errors with the rays using two different methods. The results
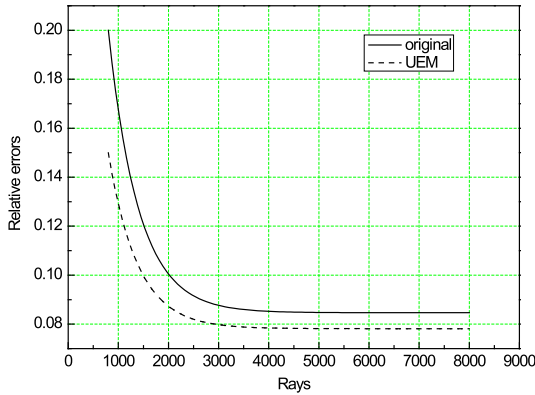
FIGURE 7. Comparison of the relative errors with the rays using two methods.

FIGURE 9. Change in reflectivity with the azimuth angle of different roughness values.

indicate that the relative errors of both methods decrease with the increase in number of rays. The relative errors of the UEM are smaller than that of the original method.

B. MULTI-LAYER DENSIFY METHOD

To further improve the efficiency of the MBTTM, the reflectivities of different roughness surfaces from different directions are investigated in this paper. The results are shown in Figures 8 and 9.
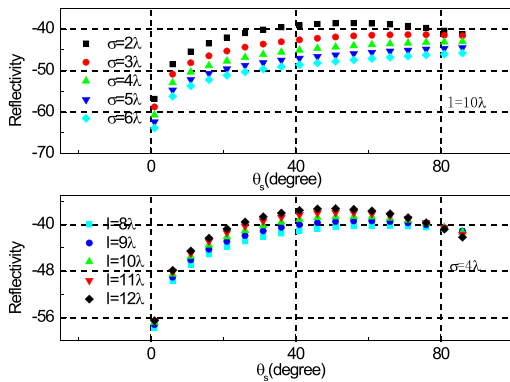

FIGURE 8. Change in reflectivity with the scattering angle of different roughness values.

In Figures 8 and 9, the incident direction is ($\theta_i = 60°$, $\varphi_i = 0°$). The results in Figure 8 show that the reflectivity of the rough surface increases with the scattering angle to a maximum value; then, it decreases with the scattering angle. The rough surface obtains the extremal reflectivity when the scattering angle is equal to the reflection angle.

In Figure 9, the change curves of the reflectivity are divided by the symmetry axis $\varphi_s = 180°$; when $\varphi_s = 0°$, the reflectivity is maximal. Thus, the reflectivity is much higher near the reflection direction than away from the reflection direction. The densified area is shown in blue in Figure 10. To further increase the usage of the rays, we densify the rays near the reflection direction.
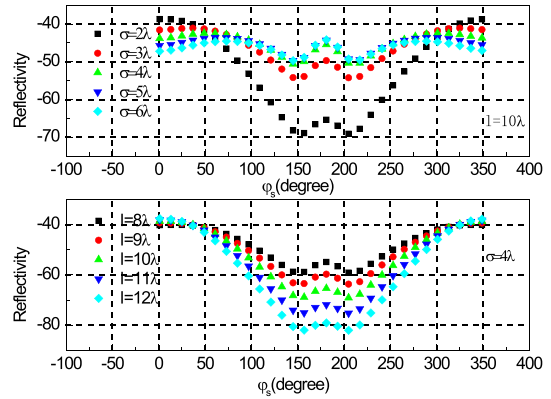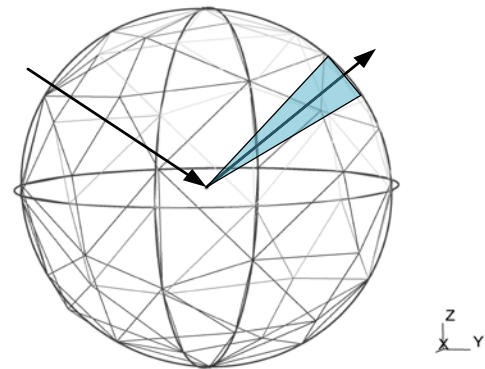

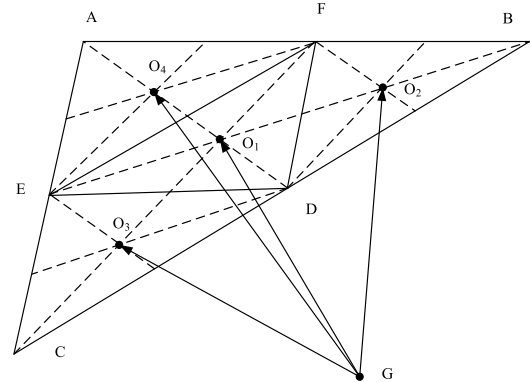FIGURE 10. Densified area near the reflection direction.

FIGURE 11. Model of the MLDM with one layer.

To assure that the new rays are uniformly distributed, a new method called MLDM is proposed in this paper. Figure 10 shows the model of one layer.

In Figure 11, triangle ABC is a meshed unit on the sphere surface, point G is the center point of the sphere, and $\overrightarrow{GO_1}$ is the direction of the original ray, where point O_1 is the center point of the triangle. Points E, F, and D are the midpoints of the three sides. Points O_2, O_3, and O_4 are the center pointes of the new triangles. Hence, $\overrightarrow{GO_2}$, $\overrightarrow{GO_3}$, and $\overrightarrow{GO_4}$ are the

FIGURE 12. Model of the MLDM with two layers.

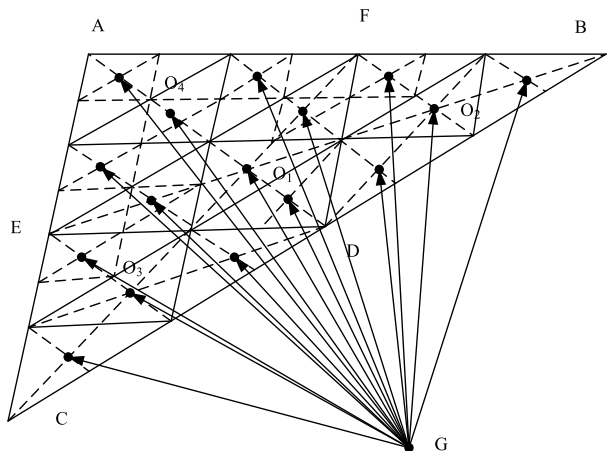**FIGURE 13.** Order of the points.

directions of the new rays. Figure 12 shows the model of the MLDM with two layers.

The detail of the MLDM is as follows.

- We assume the number of layers to be N, and the coordinate of the three vertices of the meshed unit can be represented in a matrix $e(3, 3)$.
- The total number of rays in the triangle region is denoted by nzi. The number of points on two sides of the triangle is n; the total number of points in the triangle region is nz. We have

$$\begin{cases} nzi = 4^N \\ n = 2^N + 1 \\ nz = \dfrac{(n+1) \cdot n}{2} \end{cases} \quad (5)$$

- The coordinate matrices of the points on the two sides are $a(3, n)$ and $b(3, n)$, which can be obtained by

$$\begin{cases} a(j, o) = \dfrac{o - 1}{2^N} \cdot a(j, 1) + \dfrac{n - o}{2^N} a(j, n) \\ b(j, o) = \dfrac{o - 1}{2^N} \cdot b(j, 1) + \dfrac{n - o}{2^N} b(j, n) \\ a(j, 1) = b(j, 1) = e(j, 1) \\ \qquad (j = 1, 2, 3; o = 1, 2, 3 \ldots 2^N) \\ a(j, n) = e(j, 2) b(j, n) = e(j, 3) \end{cases} \quad (6)$$

- The raw order of the points is shown in Figure 13, and it is difficult to compute the ray direction. To ease the work, the order of the points was rearranged as shown in Figure 14.
- After $a(3, n)$ and $b(3, n)$ have been obtained, the coordinate matrix of the points in the triangle region is $c(3, nz)$, which can be obtained by the combination and weighting of $a(3, n)$ and $b(3, n)$.
- Finally, the directions of the rays are obtained by $c(3, nz)$.

Combing the MLDM with the MBTTM, we can promote the efficiency of the imaging simulation of the rough surface scene.
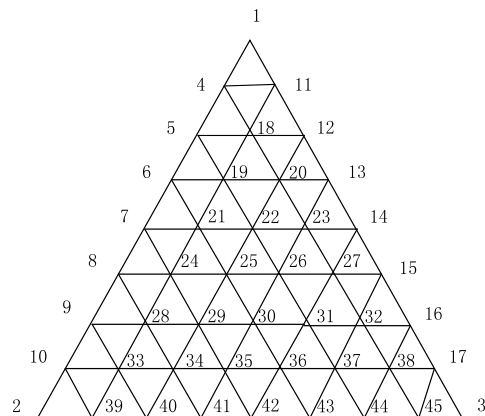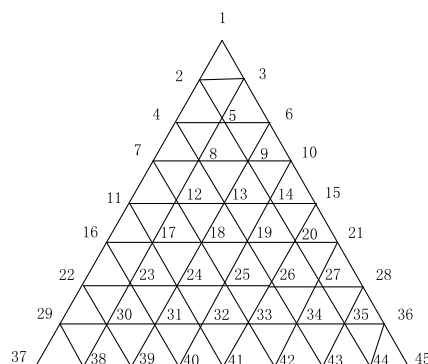

FIGURE 14. Rearranged order of the points.
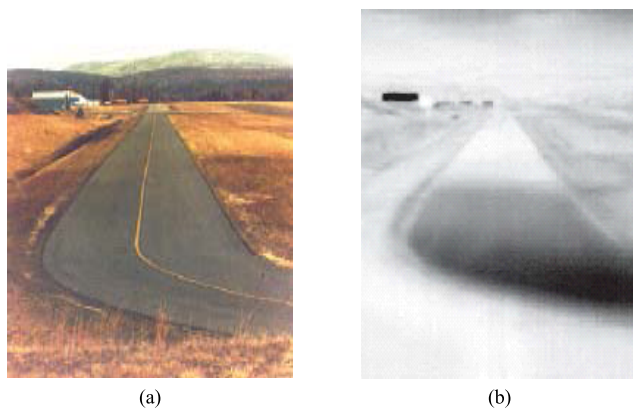

(a)   (b)

FIGURE 15. Optical and measured image of an airplane runway.

IV. EXPERIMENTAL RESULTS

A. EXPERIMENT OF AN ACTUAL SCENE

To prove the correctness and high efficiency of the new approach, we simulate the scene of an airplane runway using the proposed method. The optical and measured images of the airplane runway are shown in Figures 15(a) and (b) [28].

The model and simulated image of the airplane runway are shown in Figures 16 and 17. In the model, the runway is an asphalt road, the roof of the warehouse is metal, and the field
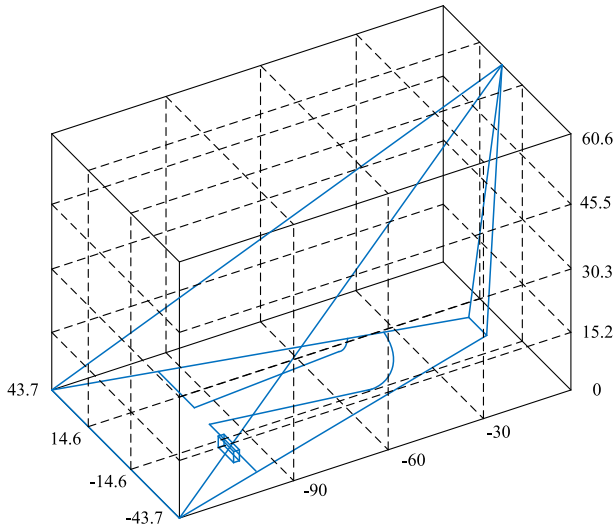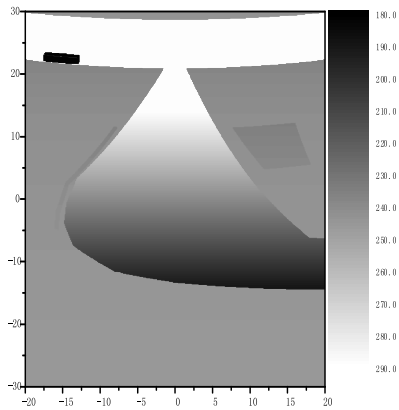
FIGURE 16. Model of the airplane runway.

FIGURE 17. Simulated image of the airplane runway.

FIGURE 18. Measured scene of the grass.

FIGURE 19. Comparison of the new method with the measured value.

next to the runway is grass with two different roughness values. In the calculation, the work frequency of the radiometer is 94 GHz; the lengths of the long grass and short grass are set as 20 λ and 3.5 λ.

The simulated image clearly reproduces the measured image of the radiometer accurately; however, there is a slight difference between the measured image and the simulated image because of the scene modeling.

To further improve the correctness of the new method, we measure the brightness temperature of grass using a radiometer antenna. Figure 18 shows the grass scene measured using a millimeter radiometer. The results are shown in Figure 19. For convenient comparison, the calculated results that use the new method are also shown in Figure 19.

The working frequency is 94 GHz, the spatial resolution is 0.5°, and the temperature resolution is 1K. The root mean square height and correlation length are 3.5λ and 10λ. The results reveal that the value obtained by the new method is essentially consistent with the measured value; the errors may originate from the inexactness of the details of the scene, such as media and background parameters.
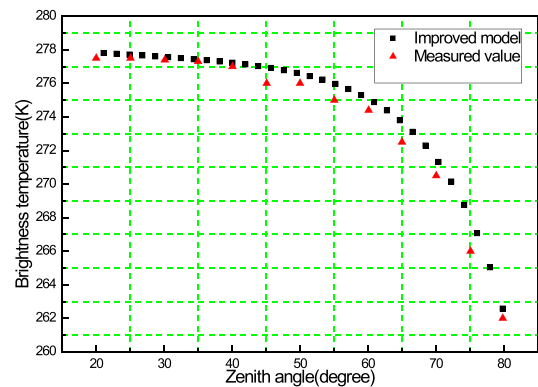
Hence, we can conclude that the new method is applicable in simulating the image of a rough surface.

B. ANALYSIS OF THE RESULTS

To study the effect of the densified area on the simulation results, three different densified areas are compared in this paper: (50° < θ < 70°, −10° < φ < 10°), (40° < θ < 80°, −20° < φ < 20°) and (30° < θ < 90°, −30° < φ < 30°). The results are shown in Figure 20. The work parameters are the same as Figure 19.

In Figure 20, to assure the comparability of the results, the three curves are obtained using MDLM with one layer. The results indicate that the relative errors decrease with the number of rays, but the three densified areas have different descending slopes. When the same number of rays is used, the relative error of 20° is the lowest in the three curves, and the relative error of 10° is the highest.

Therefore, the relative error does not continue to decrease with the increase in densified area. To characterize the effect of the densified area on the MLDM, an ODA (optimum densified area) is defined in this paper based on the roughness. For a complicated scene with a rough surface, when the densified area is smaller than the ODA, the relative errors decrease with the densified area; however, when the densified area is larger than the ODA, the relative errors increase with the densified area.
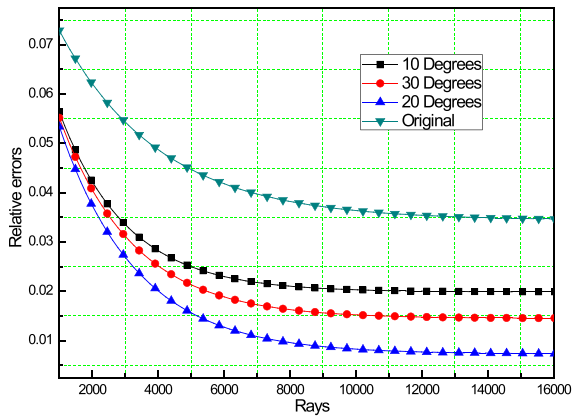
FIGURE 20. Comparison of the relative errors with the rays of different densified areas.
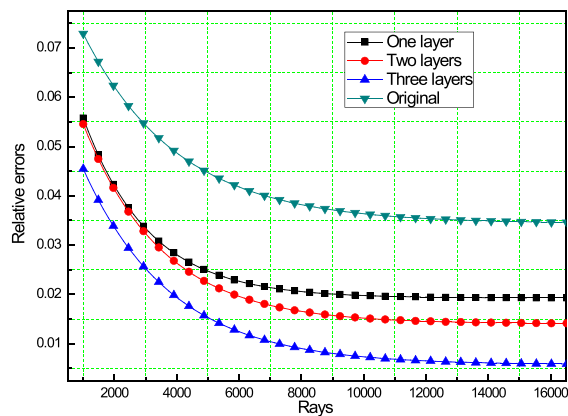

FIGURE 21. Comparison of the relative errors with the rays of different numbers of densified layers.

To study the effect of the number of layers on the simulation results, different numbers of layers are calculated and compared in Figure 21. The work frequency of the radiometer is 94 GHz, and the densified area is ($50° < \theta < 70°$, $-10° < \varphi < 10°$).

The results in Figure 21 reveal that the relative errors decrease with the number of rays. When the same number of rays is used, the relative errors decrease with the number of densified layers in the simulation.

To study the effect of the roughness on the layers and densified area used in the calculation, two different rough surfaces are compared in Figure 22. In the calculation, the work parameters are the same as Figure 19 and 8000 rays are used. The roughness of the two rough-surfaces are ($\sigma = 3.5\lambda$, $l = 10\lambda$) and ($\sigma = 2.5\lambda$, $l = 15\lambda$).

The results indicate that the two rough surfaces both decrease with the layers calculated in the simulation. However, various roughness has different descending slopes. Moreover, the ODAs of the two rough-surfaces are marked in Figure 22, and the results show that the ODA increase with the roughness.

Finally, to demonstrate the high efficiency of the fast MBTTM, two methods are used to simulate the scene in Figure 5. The results are shown in Figures 23 and 24.
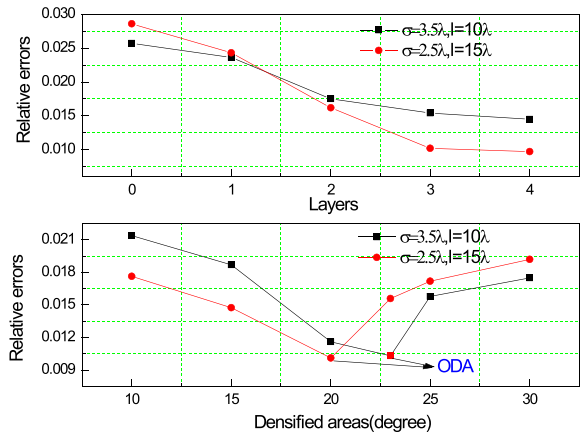

FIGURE 22. Comparison of the relative errors with the layers and densified areas of different roughness.
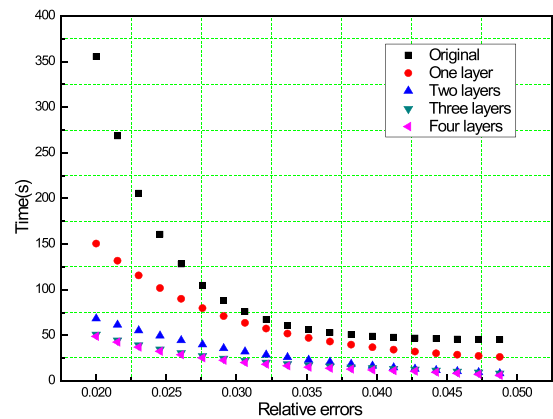
FIGURE 23. Comparison of the computing time with the relative errors using different numbers of densified layers.

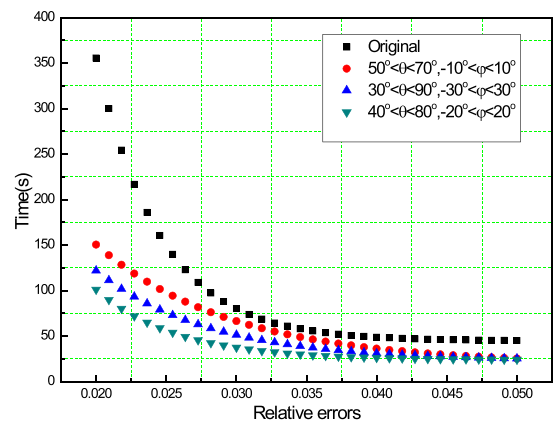**FIGURE 24.** Comparison of the computing time with the relative errors using different densified areas.

In Figure 23, the densified area is ($50° < \theta < 70°$, $-10° < \varphi < 10°$), and the two methods are compared in terms of computing time. The results indicate that the computing time using the fast MBTTM is clearly shorter than that using the original MBTTM. The computing time decreases with

the number of layers. When the number of layers increases from three to four, the two curves almost coincidence with each other, which implies that three layers are sufficient for this scene. The computing time of the fast MBTTM almost linearly increases with the decrease in relative errors.

Figure 24 compares the computing time of different densified areas. The results also indicate that the fast MBTTM is more efficient than the original MBTTM. When the densified areas are ($40° < \theta < 80°$, $-20° < \varphi < 20°$), the computing time is the shortest; when the densified areas extend to ($30° < \theta < 90°$, $-30° < \varphi < 30°$), the computing time increases. This result is consistent with the aforementioned conclusion.

V. CONCLUSIONS

A fast MBTTM is proposed in this paper for the Passive MMW simulation of rough-surface scenes. The new method significantly reduces the number of rays in the sub-layer calculation and promotes the efficiency of utilization of the rays. By comparing with the measurement results, it can be indicated that the proposed method can be applicable in simulating the image of a rough surface.

In addition, the effect of the densified area and the number of densified layers on the relative errors are also been studied. The relative error does not continue decreasing with the increase in densified area. When the densified area is smaller than the ODA, the relative error decreases with the densified area; however, when the densified area is larger than the ODA, the relative error increases with the densified area. The results in this paper imply that the relative error decreases with the number of layers in the simulation. Furthermore, the results indicate that the proposed fast MBTTM can significantly increases the efficiency of the simulation of complicated scenes that contain rough surfaces. However, the fast MBTTM proposed in this paper is not perfect: the ODA is related to the roughness and material of the rough surface. Therefore, a useful theoretical formula is required to compute the ODA, which will be discussed in future studies.

REFERENCES

[1] G.-D. Liu and Y.-R. Zhang, "Three-dimensional microwave-induced thermo-acoustic imaging for breast cancer detection," *Acta Phys. Sinica*, vol. 60, pp. 074303-1–074303-7, Jul. 2011.

[2] W. J. Ji and C. M. Tong, "Research on electromagnetic scattering computation and synthetic aperture radar imaging of ship located on two-dimensional ocean surface," *Acta Phys. Sinica*, vol. 61, no. 16, pp. 160301-1–160301-8, 2012.

[3] K. Dai et al., "Extracting vertical displacement rates in Shanghai (China) with multi-platform SAR images," *Remote Sens.*, vol. 7, no. 8, pp. 9542–9562, 2015.

[4] A. Gorrab, M. Zribi, N. Baghdadi, B. Mougenot, P. Fanise, and Z. L. Chabaane, "Retrieval of both soil moisture and texture using TerraSAR-X images," *Remote Sens.*, vol. 7, no. 8, pp. 10098–10116, 2015.

[5] N. Gopalsami, S. Liao, T. Elmer, E. R. Koehl, and A. C. Raptis, "Evaluation of passive millimeter wave system performance in adverse weather conditions," *Proc. SPIE*, vol. 8362, pp. 83620I-1–83620I-6, May 2012.

[6] S. Liao et al., "Passive millimeter-wave dual-polarization imagers," *IEEE Trans. Instrum. Meas.*, vol. 61, no. 7, pp. 2042–2050, Jul. 2012.

[7] N. Gopalsami et al., "Passive millimeter-wave imaging with compressive sensing," *Opt. Eng.*, vol. 51, no. 9, pp. 091614-1–091614-9, 2012.

[8] N. Gopalsami, S. Liao, T. Elmer, A. Heifetz, and A. C. Raptis, "Compressive sampling in active and passive millimeter-wave imaging," in *Proc. Int. Conf. Infr., Millim. THz Waves*, Oct. 2011, pp. 1–2.

[9] G. Zhang, X. Li, and G. Lou, "Research on passive MMW imaging based on an alternating current radiometer," *J. Infr. Millim. Waves.*, vol. 26, no. 6, pp. 461–464, 2007.

[10] Y.-D. Zhang, Y.-S. Jiang, Y.-T. He, and H.-Y. Wang, "Passive millimeter-wave imaging using photonic processing technology," *J. Infr. Millim. Waves.*, vol. 30, no. 6, pp. 551–555, 2011.

[11] S. I. Khan, Y. Hong, J. J. Gourley, M. U. Khattak, and T. De Groeve, "Multi-sensor imaging and space-ground cross-validation for 2010 flood along Indus River, Pakistan," *Remote Sens.*, vol. 6, no. 3, pp. 2393–2407, 2014.

[12] C. S. Ruf, C. T. Swift, A. B. Tanner, and D. M. Le Vine, "Interferometric synthetic aperture microwave radiometry for the remote sensing of the Earth," *IEEE Trans. Geosci. Remote Sens.*, vol. 26, no. 5, pp. 597–611, Sep. 1988.

[13] L. Yujiri, "Passive millimeter wave imaging," in *IEEE MTT-S Int. Microw. Symp. Dig.*, vol. 4. Jun. 2006, pp. 98–101.

[14] M. R. Fetterman, J. Dougherty, and W. L. Kiser-Suffix, Jr., "Scene simulation of millimeter-wave images," in *Proc. IEEE Antennas Propag. Soc. Int. Symp.*, Jun. 2007, pp. 1493–1496.

[15] K. Williams et al., "Ray tracing for simulation of millimeter-wave whole body imaging systems," *IEEE Trans. Antennas Propag.*, vol. 63, no. 12, pp. 5913–5918, Dec. 2015.

[16] K. Williams, L. Tirado, Z. Chen, B. Gonzalez-Valdes, J. Á. Martínez-Lorenzo, and C. M. Rappaport, "Ray tracing simulation tool for portal-based millimeter-wave security systems using the NVIDIA OptiX ray tracing engine," in *Proc. Radio Sci. Meeting*, Jul. 2013, p. 167.

[17] M. Dong, W.-M. Chan, T. Kim, K. Liu, H. Huang, and G. Wang, "Simulation study on millimeter wave 3D beamforming systems in urban outdoor multi-cell scenarios using 3D ray tracing," in *Proc. Int. Symp. Pers., Indoor, Mobile Radio Commun.*, Aug. 2015, pp. 2265–2270.

[18] B. Göktepe, M. Peter, R. J. Weiler, and W. Keusgen, "The influence of street furniture, tree trunks, and traffic in urban scenarios on ray tracing simulations in the millimeter wave band," *Int. J. Microw. Wireless Technol.*, vol. 8, nos. 4–5, pp. 785–793, 2016.

[19] N. A. Salmon, R. Appleby, and S. Price, "Scene simulation of passive millimeter-wave images of plastic and metal objects," *Proc. SPIE*, vol. 4719, pp. 397–401, Jul. 2002.

[20] N. A. Salmon, "Polarimetric scene simulation in millimeter-wave radiometric imaging," *Proc. SPIE*, vol. 5410, pp. 260–269, Aug. 2004.

[21] N. A. Salmon, "Polarimetric passive millimeter-wave imaging scene simulation including multiple reflections of subjects and their backgrounds," *Proc. SPIE*, vol. 5989, p. 598917, Nov. 2005.

[22] C. Zhang and J. Wu, "Near field 3D scene simulation for passive microwave imaging," *Proc. SPIE.*, vol. 6419, p. 641902, Oct. 2006.

[23] C. Zhang and J. Wu, "Image simulation for ground objects microwave radiation," *J. Electron. Inf. Technol*, vol. 29, no. 11, pp. 2725–2728, 2007.

[24] M. R. Fetterman, J. Grata, G. Jubic, W. L. Kiser-Suffix, Jr., and A. Visnansky, "Simulation, acquisition and analysis of passive millimeter-wave images in remote sensing applications," *Opt. Exp.*, vol. 16, no. 25, pp. 20503–20515, 2008.

[25] B. Qi et al., "Passive millimeter-wave scene imaging simulation based on fast ray-tracing," in *Proc. IEEE Geosci. Remote Sens. Symp.*, Jul. 2016, pp. 2642–2645.

[26] L.-Y. Chang, C.-C. Nien, C.-M. Li, C.-Y. Huang, Y.-C. Yu, and J.-H. Tarng "A simulation method of image construction for passive millimeter-wave imaging system," in *Proc. IEEE Convent. Elect. Electron. Eng. Israel*, Nov. 2010, pp. 713–716.

[27] N. A. Salmon and P. R. Coward, "Scattering in polarimetric millimetre-wave imaging scene simulation," *Proc. SPIE.*, vol. 6211, p. 621107, May 2006.

[28] F. T. Ulaby, R. K. Moore, and A. K. Fung, *Microwave Remote Sensing Active and Passive-Volume III: From Theory to Applications*, vol. 22. Norwood, MA, USA: Artech House, 1986, pp. 1223–1227.

[29] C. Yin, M. Zhang, and Y. Bo, "Multilayer brightness temperature tracing method for rough surface scene simulation in passive millimeter-wave imaging," *Int. J. Antennas Propag.*, vol. 2016, Sep. 2016, Art. no. 6763182.

[30] C. Yin, M. Zhang, and Y. Bo, "Simulation of multi-layer rough surfaces media in the passive millimeter-wave imaging," *Progr. Electromagn. Res. M*, vol. 51, pp. 51–62, Oct. 2016.

[31] L. Zhou, L. Tsang, V. Jandhyala, Q. Li, and C. H. Chan, "Emissivity simulations in passive microwave remote sensing with 3-D numerical solutions of Maxwell equations," *IEEE Trans. Geosci. Remote Sens.*, vol. 42, no. 8, pp. 1739–1748, Aug. 2004.
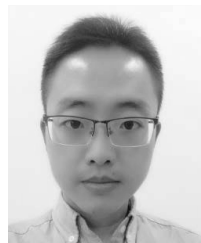
CHUAN YIN was born in Chaohu, China, in 1987. He received the Ph.D. degree in electromagnetic field and microwave technology from the Nanjing University of Post and Telecommunication, Nanjing, China, in 2016.

He is currently a Lecturer with the School of Electronics and Information, Hangzhou Dianzi University. His main research interests include imaging in passive millimeter wave, optimization algorithm, and filtering antennas.

YOULIN GENG received the M.Sc. degree in electromagnetic field and microwave techniques from the China Research Institute of Radiowave Propagation (CRIRP), Xinxiang, China, in 1992, and the Ph.D. degree in electronic science and technology from Xidian University, Xian, China, in 2006. From 1992 to 2002, he was with the CRIRP as an Assistant Engineer, an Engineer, and a Senior Engineer. Since 2002, he has been with the Institute of Antennas and Microwaves, Hangzhou Dianzi University, Hangzhou, China, as a Faculty Member, where he has been a Full Professor Since 2005.

His current research interests include analytical and numerical methods of electromagnetic scattering by complex media, and wave propagation in complex medium. He is a Senior Member of the Chinese Institute of Electronics.
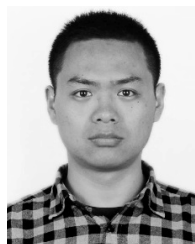
YUJIAN PAN received the B.S. degree in vacuum electronics technology from the University of Electronic Science and Technology of China, Chengdu, China, in 2010, and the M.S. and Ph.D. degrees in electronic science and technology from the National University of Defense Technology, Changsha, China, in 2012 and 2015, respectively.

He is currently a Lecturer with the School of Electronics and Information, Hangzhou Dianzi University, Hangzhou, China. His research interests include array signal processing, sparse reconstruction, and radar signal processing.
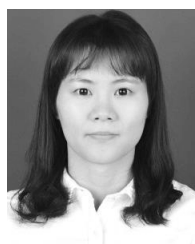
HUAYAN JIN was born in Hangzhou, China, in 1989. She received the B.S. degree in electronic engineering and the Ph.D. degree in electromagnetic field and microwave technology from the Nanjing University of Science and Technology, Nanjing, China, in 2011 and 2017, respectively.

In 2012, 2013, and 2014, she was an Exchange Student at the Chang Gung University, Taoyuan, Taiwan. She is currently a Lecturer with the School of Electronics and Information, Hangzhou Dianzi University. Her main research interests include differential-fed antennas, wideband microstrip antennas, millimeter-wave antennas and filtering antennas. She serves as a Reviewer of the *IET Electronics Letters*.

● ● ●